Article

Facial Symmetry in Protein Self-Assembly

Anil K. Mehta, Kun Lu, W. Seth Childers, Yan Liang, Steven N. Dublin, Jijun Dong, James P. Snyder, Sai Venkatesh Pingali, Pappannan Thiyagarajan, and David G. Lynn

J. Am. Chem. Soc., **2008**, 130 (30), 9829-9835 • DOI: 10.1021/ja801511n • Publication Date (Web): 02 July 2008

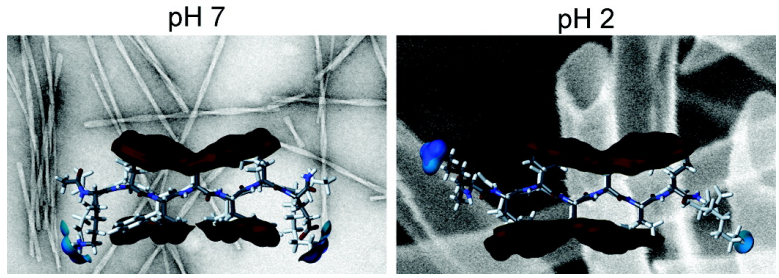

J|A|C|S
ARTICLES

Published on Web 07/02/2008

Facial Symmetry in Protein Self-Assembly

Anil K. Mehta,[†] Kun Lu,[*,†] W. Seth Childers,[†] Yan Liang,[†] Steven N. Dublin,[†] Jijun Dong,[†] James P. Snyder,[*,†] Sai Venkatesh Pingali,[‡] Pappannan Thiyagarajan,[*,‡] and David G. Lynn[*,†]

Center for the Analysis of Supramolecular Self-assemblies, Departments of Chemistry and Biology, Emory University, Atlanta, Georgia 30322, and Intense Pulsed Neutron Source, Argonne National Laboratory, Argonne, Illinois 60439

Received February 28, 2008; E-mail: david.lynn@emory.edu

Abstract: Amyloids are self-assembled protein architectures implicated in dozens of misfolding diseases. These assemblies appear to emerge through a "selection" of specific conformational "strains" which nucleate and propagate within cells to cause disease. The short Aβ(16−22) peptide, which includes the central core of the Alzheimer's disease Aβ peptide, generates an amyloid fiber which is morphologically indistinguishable from the full-length peptide fiber, but it can also form other morphologies under distinct conditions. Here we combine spectroscopic and microscopy analyses that reveal the subtle atomic-level differences that dictate assembly of two conformationally pure Aβ(16−22) assemblies, amyloid fibers and nanotubes, and define the minimal repeating unit for each assembly.

Introduction

The cross-β scaffold[1] that characterizes the micrometers long, 50−100 Å diameter, unbranched amyloid assemblies[2] places peptide β-strands perpendicular to the long fiber axis. This architecture is quite possibly accessible to all proteins[3] and, increasingly in the context of certain disease states, has been associated with distinct strains or subtypes.[4−9] For example, the Aβ peptide associated with Alzheimer's disease forms self-propagating amyloid fibers with different morphologies under slightly different culture conditions, and these differences are reflected in their neuronal toxicity.[10] The transmission efficiency of the *Saccharomyces cerevisiae* prion protein Sup35 also tracks with fiber morphology,[4,11−13] and environmental conditions, such as the presence of metal ions, can critically impact both assembly and neurotoxicity of the human prion PrP[14] and Aβ(13−21)[15] (a nine residue fragment of Aβ). While the toxic strains may provide targets for therapeutic intervention, little is known about the structural differences that distinguish these assemblies.

Many amyloidogenic proteins contain simple repeats of 6−8 amino acids which have been implicated in nucleating assembly.[8,9,16] For example, the central "cassette" from the Aβ peptide, Ac-KLVFFAE-NH_2 or Aβ(16−22), at neutral pH assembles as mixtures of both fibers and homogeneous diameter nanotubes.[17] *In vitro* conditions have been determined in which Aβ(16−22) assembles into either fibers or nanotubes, and, most importantly, each superstructure can be interconverted when conditions are reversed. The structural models developed here define the basis for the morphological selection[18]and reveal some of the critical energetic contributors that define each morphology.

Materials and Methods

Peptides were synthesized using standard NMM/HBTU protocols for Fmoc solid-phase synthesis. ^{13}C- and ^{15}N-labeled amino acids were purchased from CIL (Andover, MA). Peptides were RP-HPLC purified to >98%. MALDI-TOF with a 2,5-dihydroxybenzoic acid matrix confirmed molecular weight. Peptides were dissolved in 40%

[†] Emory University.
[‡] Argonne National Laboratory.

(1) Geddes, A. J.; Parker, K. D.; Atkins, E. D. T.; Beighton, E. *J. Mol. Biol.* **1968**, *32*, 343–358.
(2) Eanes, E. D.; Glenner, G. G. *J. Histochem. Cytochem.* **1968**, *16*, 673–677.
(3) Chiti, F.; Webster, P.; Taddei, N.; Clark, A.; Stefani, M.; Ramponi, G.; Dobson, C. M. *Proc. Natl. Acad. Sci. U.S.A.* **1999**, *96*, 3590–3594.
(4) Tanaka, M.; Chien, P.; Naber, N.; Cooke, R.; Weissman, J. S. *Nature* **2004**, *428*, 323–328.
(5) Jones, E. M.; Surewicz, W. K. *Cell* **2005**, *121*, 63–72.
(6) Ritter, C.; Maddelein, M. L.; Siemer, A. B.; Luhrs, T.; Ernst, M.; Meier, B. H.; Saupe, S. J.; Riek, R. *Nature* **2005**, *435*, 844–848.
(7) Riek, R. *Nature* **2006**, *444*, 429–431.
(8) Dong, J.; Lu, K.; Lakdawala, A. S.; Mehta, A. K.; Lynn, D. G. *Amyloid* **2006**, *13*, 206–215.
(9) Sawaya, M. R.; Sambashivan, S.; Nelson, R.; Ivanova, M. I.; Sievers, S. A.; Apostol, M. I.; Thompson, M. J.; Balbirnie, M.; Wiltzius, J. J.; McFarlane, H. T.; Madsen, A. O.; Riekel, C.; Eisenberg, D. *Nature* **2007**, *447*, 453–457.
(10) Petkova, A. T.; Leapman, R. D.; Guo, Z.; Yau, W. M.; Mattson, M. P.; Tycko, R. *Science* **2005**, *307*, 262–265.
(11) Derkatch, I. L.; Chernoff, Y. O.; Kushnirov, V. V.; Inge-Vechtomov, S. G.; Liebman, S. W. *Genetics* **1996**, *144*, 1375–1386.
(12) Krishnan, R.; Lindquist, S. L. *Nature* **2005**, *435*, 765–772.
(13) Toyama, B. H.; Kelly, M. J.; Gross, J. D.; Weissman, J. S. *Nature* **2007**, *449*, 233–237.
(14) Millhauser, G. L. *Acc. Chem. Res.* **2004**, *37*, 79–85.
(15) Dong, J.; Canfield, J. M.; Mehta, A. K.; Shokes, J. E.; Tian, B.; Childers, W. S.; Simmons, J. A.; Mao, Z.; Scott, R. A.; Warncke, K.; Lynn, D. G. *Proc. Natl. Acad. Sci. U.S.A.* **2007**, *104*, 13313–13318.
(16) Dong, J.; Bloom, J. D.; Goncharov, V.; Chattopadhyay, M.; Millhauser, G. L.; Lynn, D. G.; Scheibel, T.; Lindquist, S. *J. Biol. Chem.* **2007**, *282*, 34204–34212.
(17) Lu, K.; Jacob, J.; Thiyagarajan, P.; Conticello, V. P.; Lynn, D. G. *J. Am. Chem. Soc.* **2003**, *125*, 6391–6393.
(18) Lynn, D. G.; Snyder, J. P.; Lakdawala, A. S.; Dong, J.; Lu, K. *Structure* **2003**, *11*, 242.
(19) Lu, K.; Guo, L.; Mehta, A. K.; Childers, W. S.; Dublin, S. N.; Skanthakumar, S.; Conticello, V. P.; Thiyagarajan, P.; Apkarian, R. P.; Lynn, D. G. *Chem. Commun. (Cambridge)* **2007**, 2729–2731.

CH_3CN/water with 0.1% TFA (pH ~2.1) to a final concentration of 1.3 mM. For nanotubes, the pH was maintained at 2 and adjusted to ~6−7 with 0.1 M NaOH 40% CH_3CN/water for fibers. Samples were allowed to self-assemble and mature for 2 weeks.

Cryo-Etch High-Resolution SEM. The nanotube solution was plunge-frozen in liquid ethane, transferred to a precooled (−170 °C) Gatan 3500 CT cryostage, fractured with a prechilled blade, and washed with liquid nitrogen. The cryostage was transferred to a Denton DV-602 Cr coater. The temperature was increased to −105 °C and held for 20−30 min at 0.2 μTorr to allow exposed ice to sublime (etch). The sample was then cooled to −170 °C and sputter-coated with Cr at a rate of 0.3 Å/s and a current of 50 mA at 300 V under 5 mTorr Ar atmosphere, resulting in a 2 nm Cr film. The Cr-coated sample was transferred in-lens to a DS-130F field emission scanning electron microscope. The cryostage temperature was ramped slowly to −120 °C and equilibrated for 30 min.

Electron Diffraction. Diffraction patterns were recorded using a Philips 410 EM transmission electron microscope in diffraction mode. *d*-spacing was calculated with $d = \lambda L/R$, where R is the distance (mm) from the central bright spot to the arc of interest, L is the camera length (distance in mm between specimen and photographic film), and λ is the electron wavelength (80 kV = 4.2 pm). Camera length was calibrated using an aluminum polycrystalline standard (Electron Microscopy Sciences, Hartfield, PA).

FTIR. [1-^{13}C]-labeled peptides, assembled as fibers or nanotubes, were induced to macroassemble with the addition of 18 mM Na_2SO_4. The samples were pelleted, lyophilized, and prepared as KBr pellets with equal weights for analysis.

Solid-State NMR. All NMR spectra were collected with a Bruker (Billerica, MA) Avance 600 spectrometer and a Bruker 4 mm HXY magic-angle spinning (MAS) probe. To compensate for pulse imperfections, xy8 phase cycling[20] of ^{13}C{^{15}N} REDOR 6 and 10 μs rotor-synchronized ^{13}C and ^{15}N π pulses, respectively, and EXORCYCLE phase cycling[21,22] of the final ^{13}C Hahn-echo refocusing pulse were applied with 95 kHz Spinal64[23] ^{1}H decoupling. MAS frequency was kept under active control at 10 kHz ± 2 Hz. The cooling and spinning air exit temperature was maintained below −1 °C to ensure MAS and RF heating did not denature the samples. ^{13}C (150.8 MHz) and ^{15}N (60.8 MHz) CP-MAS spectra before and after REDOR experiments confirmed that the samples did not change during the experiment. Nanotubes were protected[19] by precipitating with SO_4^{2-} in the presence of 30 mM trehalose, 0.67 mg/mL dextran (81.5 and 488 kDa), and 1% PEG-8000, which acted as cryo- and lyo-protectants. TEM confirmed the presence of only intact tubes after lyophilization.

REDOR data points are the sum of center- and sideband peak-heights. Error bars were calculated using the noise of each spectrum as the maximum peak height deviation. To match the X-ray-determined distance for room-temperature ^{13}C{^{15}N} REDOR of [1-^{13}C,^{15}N]glycine diluted 10:1 with natural abundance glycine, the calculated REDOR curve was scaled[24] by a factor of 0.86 to account for imperfect ^{13}C and ^{15}N π pulses (Figure S3). With this scaling factor, the REDOR-determined ^{13}C−^{15}N internuclear distance is 2.5 ± 0.1 Å, which compares well to the X-ray-determined distance of 2.49 Å.[25] This scaling factor was applied to all calculated REDOR curves. To ensure that this scaling factor did not change over the course of the experiments, ^{13}C{^{15}N} REDOR measurements were made on the diluted [1-^{13}C,^{15}N]-glycine sample before and after every Aβ(16−22) sample. REDOR simulations for intermolecular ^{13}C−^{15}N distances account for the dephasing of a single ^{13}C spin in the presence of two ^{15}N spins[26] and do not include any ^{15}N−^{15}N dipolar coupling. A correction for natural abundance carbonyl carbons and dephasing[27] of the natural abundance carbonyl carbons adjacent to the labeled ^{15}N's was also included.

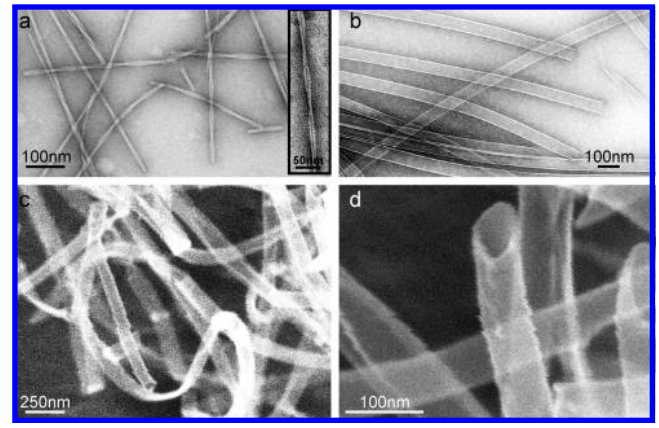

Figure 1. Assembly of Aβ(16−22) peptide fibers and nanotubes in 40% acetonitrile. TEM micrograph of (a) fibers formed at pH 6 (inset shows twisted fiber dimer, scale bar = 50 nm) and (b) tubes at pH 2. Cryo-etch high-resolution SEM images of nanotubes with homogeneous diameters (scale bar = 250 nm) (c) and hollow cross-sections (d).

Molecular Dynamics. Initial peptide registry for MD simulations matched the ^{13}C{^{15}N} REDOR data for both the tubes and the fibers. A total of five sheets, each consisting of five peptides, were stacked on top of each other in various conformations (Figure S6). Unrestrained MD was carried out with the GROMACS 3.2 software package[28] at 300 K and 1 bar in an octahedral box of SPC water[29] with periodic boundary conditions using the all-atom OPLS-AA force field.[30] Bond distances were constrained with the LINCS algorithm,[31] and an integration time step of 2 fs was employed. Electrostatic interactions were calculated with a 1.2 Å Ewald particle mesh algorithm[32] grid spacing, a spline interpolation of 1.2 Å, and a 9 Å cutoff. Solute and solvent were separately coupled[33] to a thermostat and barostat with time constants of 0.1 and 0.5 ps, respectively. Final models were generated by 50 steps of steepest-descent *in vacuo* energy minimization of the average over the 800 ps MD evolution.

Results

Nanotubes Are Helical Cross-β Structures. Slightly acidic mixed-solvent conditions were found where pure long, unbranched amyloid fibrils assembled (Figure 1a). High-resolution transmission electron microscopy (TEM) reveals structures interpreted as two 50 Å diameter fibrils that laterally associate to form twisted fibers with a maximum observed width of 100 Å (Figure 1a, inset). In contrast, small-angle X-ray scattering

(20) Gullion, T.; Baker, D. B.; Conradi, M. S. *J. Magn. Reson.* **1990**, *89*, 479–484.
(21) Rance, M.; Byrd, R. A. *J. Magn. Reson.* **1983**, *52*, 221–240.
(22) Sinha, N.; Schmidt-Rohr, K.; Hong, M. *J. Magn. Reson.* **2004**, *168*, 358–365.
(23) Fung, B. M.; Khitrin, A. K.; Ermolaev, K. *J. Magn. Reson.* **2000**, *142*, 97–101.
(24) Jaroniec, C. P.; Tounge, B. A.; Rienstra, C. M.; Herzfeld, J.; Griffin, R. G. *J. Magn. Reson.* **2000**, *146*, 132–139.
(25) Marsh, R. E. *Acta Crystallogr.* **1958**, *11*, 654–663.
(26) Goetz, J. M.; Schaefer, J. *J. Magn. Reson.* **1997**, *127*, 147–154.
(27) Bernard, G. M.; Miskolzie, M.; Kotovych, G.; Wasylishen, R. E. *Can. J. Chem.* **2004**, *82*, 1554–1563.
(28) Lindahl, E.; Hess, B.; van der Spoel, D. *J. Mol. Model.* **2001**, *7*, 306–317.
(29) Berendsen, H. J. C.; Postma, J. P. M.; van Gunsteren, W. F.; Hermans, J. In *Intermolecular Forces*; Reidel Publishing Co.: Dordrecht, 1981; pp 331−342.
(30) Kaminski, G. A.; Friesner, R. A.; Tirado-Rives, J.; Jorgensen, W. L. *J. Phys. Chem. B* **2001**, *105*, 6474–6487.
(31) Hess, B.; Bekker, H.; Berendsen, H. J. C.; Fraaije, J. G. E. M. *J. Comput. Chem.* **1997**, *18*, 1463–1472.
(32) Essmann, U.; Perera, L.; Berkowitz, M. L.; Darden, T.; Lee, H.; Pedersen, L. G. *J. Chem. Phys.* **1995**, *103*, 8577–8593.
(33) Berendsen, H. J. C.; Postma, J. P. M.; Vangunsteren, W. F.; Dinola, A.; Haak, J. R. *J. Chem. Phys.* **1984**, *81*, 3684–3690.

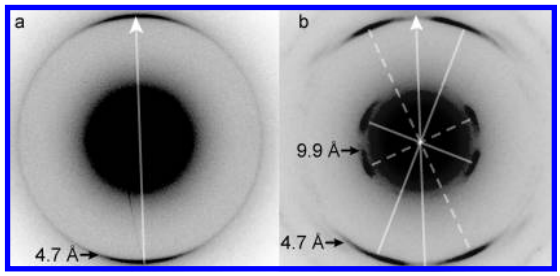

Figure 2. Electron diffraction of oriented Aβ(16−22) peptide fibers (a) and nanotubes (b). Arrows specify direction of the fiber/tube long axis with the electron beam oriented perpendicular to this axis. Dotted and solid crosses indicate independent sets of perpendicular 4.7 and 10 Å reflections. The 4.7 Å arcs of each pattern are tilted ∼23° from tube long axis. The two sets of perpendicular reflections are consistent with drying of the nanotubes on the grid.

reveals that Aβ(16−22) assembled at pH 2 resembles tubes with a 520 Å diameter and 43 Å thick walls.[17] TEM images show widths of ∼800 Å (Figure 1b), consistent with hollow tubes collapsing on the TEM grid surface after drying. Cryo-etch high-resolution scanning electron microscopy (SEM) flash-freezes the solution morphology and confirms the nanotube structure (Figure 1c,d).[19] In addition, the tubes appear flexible along their long axes and across their surfaces (Figure 1c).

Histochemical and infrared analyses found no significant structural signatures differentiating the Aβ(16−22) fibers and nanotubes from typical amyloid. Powder X-ray diffraction (XRD) of both assemblies also displayed reflections at 4.7 and 9.9 Å (see Supporting Information, Figure S1), typically assigned as the H-bonded β-strand and the β-sheet stacking repeats, respectively.[2] While both nanotubes and fibers display the strong molecular ellipticity characteristic of β-sheets (Figure S2), the $\Delta\Delta\epsilon$ values at −215 and +200 nm were significantly stronger for nanotubes. More dramatic differences appear in the electron diffraction of oriented samples. As shown in Figure 2a, the 9.9 Å reflection is too weak to be observed in the electron diffraction images of fibers but is very intense in the Aβ(16−22) nanotubes (Figure 2b). The 4.8 Å reflections in the fibers confirm that the peptide β-sheets run along the fiber long axis, characteristic of the cross-β architecture. However, nanotubes display two sets of perpendicular reflections, both with 4.8 Å arcs at an angle of 23° ± 2° with respect to the tube axis (Figure 2b). These measurements establish Aβ(16−22) nanotubes as having atypical amyloid cross-β architecture with the peptide β-sheets offset from the tube long axis.

Peptide Registry. To evaluate the relative positions of the peptide β-strands within these assemblies, [1-^{13}C]L17 and [^{15}N]A21 were synthetically incorporated into Aβ(16−22). This peptide was assembled at pH 2 and pH 6 to form nanotubes or fibers, respectively. The addition of sulfate to mature nanotubes induced formation of macroscale assemblies,[19] which facilitated drying and sample preparation of intact fibers and nanotubes. Both assemblies were harvested by centrifugation and lyophilization. The labeling scheme was selected to test for antiparallel β-sheets by measuring interstrand distances between [1-^{13}C]L17 and [^{15}N]A21 with ^{13}C{^{15}N} REDOR NMR.[34] XRD (Figure S1) defines the peptide−peptide spacing between β-sheets as 9.9 Å; therefore, intersheet cross-talk will not influence the ^{13}C−^{15}N distance measurements. Indeed, the REDOR data for fibers (Figure 3a, left) was best fit[26] to

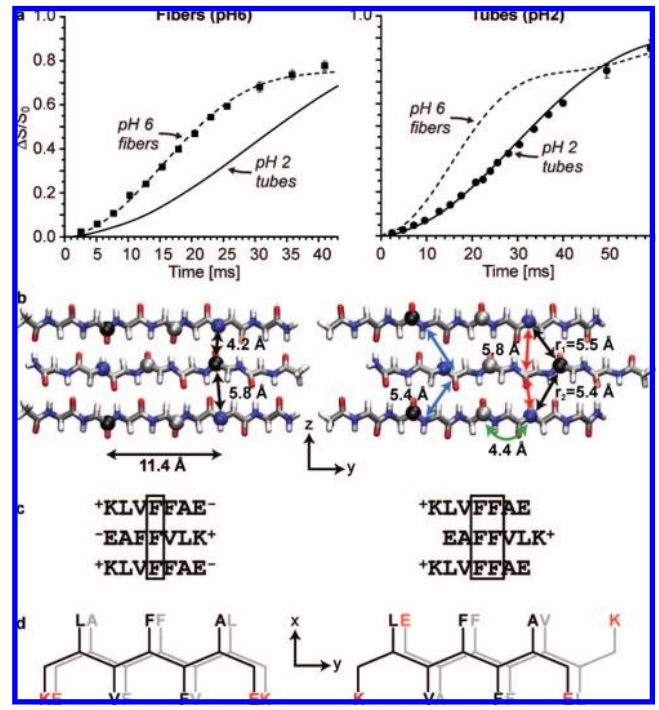

Figure 3. (a) Solid-state NMR ^{13}C{^{15}N} REDOR measurements of [1-^{13}C]L17 [^{15}N]A21 Aβ(16−22) fibers (left) and nanotubes (right). Dashed lines are calculated REDOR curves for antiparallel peptides with ^{13}C−^{15}N distances of 4.2 ± 0.2 and 5.8 ± 0.2 Å and a ^{15}N−^{13}C−^{15}N angle of 156 ± 4° (see (b), left). Solid lines are calculated REDOR curves for antiparallel out-of-register peptides with ^{13}C−^{15}N distances of 5.4 ± 0.2 and 5.5 ± 0.2 Å and an interstrand ^{15}N−^{13}C−^{15}N angle of 121° (black arrows in (b), right). In (b), only peptide backbone atoms are shown. H-bonding is along the z-axis, β-sheet stacking/lamination is along the x-axis, and β-strand extension is along the y-axis. Black spheres are L17 CO carbons, gray spheres are F19 CO carbons, and blue spheres are A21 nitrogens. The intramolecular β-strand [1-^{13}C]L17−[^{15}N]A21 distance is 11.4 Å and cannot be measured by REDOR. Also shown for tubes (b, right) are the measured intramolecular [1-^{13}C]F19−[^{15}N]A21 distance (4.4 ± 0.1 Å, green arrow)[59] and the intermolecular [1-^{13}C]V18−[^{15}N]A21 (blue arrows) and [1-^{13}C]F20 − [^{15}N]V18 (red arrows) distances (see Figure S3). (c) Sequence alignment highlighting differences in phenylalanine packing and side-chain charge. (d) Schematic β-sheet diagram showing β-sheet face sequence asymmetry for fiber (left) and symmetry for tube (right). Both tube β-sheet faces display residues K-VA-FF-EL. The front peptide is colored black, and polar residues are in red.

*inter*molecular ^{13}C−^{15}N distances of 4.2 ± 0.2 and 5.8 ± 0.2 Å, confirming H-bonding between the leucine carbonyl and alanine amide NH groups (Figure 3b−d). This same antiparallel registry has been observed for Aβ(16−22) fibers assembled at pH 7 in phosphate buffer.[35]

The peptide nanotube ^{13}C{^{15}N} REDOR data fits to longer ^{13}C−^{15}N distances of 5.4 and 5.5 Å, constraining the L17 carbonyl and A21 NH to antiparallel β-sheets, but no longer H-bonded. Rather, the peptides within the β-sheet have a one-residue registry shift (Figure 3, right). REDOR dephasing of [1-^{13}C]F19[^{15}N]A21-Aβ(16−22)-labeled peptide nanotubes (Figure S3 and green arrow in Figure 3b, right) further supports an extended β-sheet conformation, while REDOR measurements (Figure S3) on [1-^{13}C]V18[^{15}N]A21-Aβ(16−22) and [^{15}N]V18[1-^{13}C]F20-Aβ(16−22) (Figure 3b, right, blue and red arrows, respectively) confirmed the peptide registry (Figure 3c, right). This antiparallel registry corrects the originally proposed

(34) Gullion, T.; Schaefer, J. *J. Magn. Reson.* **1989**, *81*, 196–200.

(35) Balbach, J. J.; Ishii, Y.; Antzutkin, O. N.; Leapman, R. D.; Rizzo, N. W.; Dyda, F.; Reed, J.; Tycko, R. *Biochemistry* **2000**, *39*, 13748–13759.

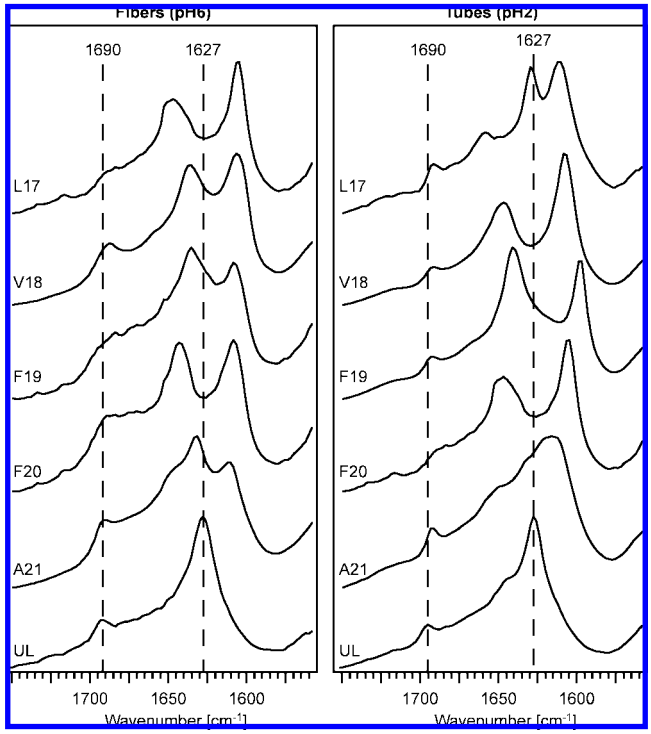

Figure 4. Amide I IR bands of unlabeled (UL) and [1-^{13}C]-enriched Aβ(16−22) fibers and nanotubes. Dashed lines through each spectrum are set at 1627 and 1690 cm^{-1}. Peak positions are listed in Table S1.

nanotube model which avoided charge burial by placing all the K16 lysines on the tube surface with parallel β-sheets.[17]

To evaluate the H-bonding alignment along the entire peptide, single ^{13}C-enriched backbone amide carbonyls were investigated via isotope-editing IR spectroscopy.[36–39] Isotopic substitution generally splits amide I bands of β-sheets into higher and lower frequency ^{12}C and ^{13}C transitions, respectively (Figure 4).[40–42] The magnitude of the ^{12}C wavelength shift depends on the extent of the perturbation of the ^{12}C carbonyl oscillator coupling network by ^{13}C substitution, and strongly coupled β-sheet regions are generally sensitive to isotopic substitution.[36,40,42] The IR spectra of unenriched Aβ(16−22) fibers and nanotubes (Figure 4, UL) both show a strong amide I absorption band at 1627 cm^{-1}, diagnostic of H-bonded β-sheet structures, and a weak absorption at ∼1690 cm^{-1}, consistent with an antiparallel configuration.[43] The additional shoulder at 1641 cm^{-1} in the nanotube IR spectrum was assigned to the flexible non-H-bonded peptide N-terminus.

The ^{13}C stretch for both fibers and nanotubes displays the anomalous intensity increase expected for antiparallel β-sheets.[40] In the L17-labeled peptide, the ^{13}C stretch shifts to ∼1610 cm^{-1} for both morphologies, while the ^{12}C signal remains almost unchanged in nanotubes but is blue-shifted ∼17 cm^{-1} in the fibers, consistent with the L17 carbonyl being in a more tightly coupled network in fibers than in nanotubes (Figure 3b,c). ^{13}C-carbonyl V18 and F20 labels in nanotubes have IR spectra similar to those of the V18, F19, and F20 labels in fibers, consistent with highly ordered central regions. However, the F19 ^{13}C transition in nanotubes shifts to 1596 cm^{-1}, close to the theoretically calculated 35 cm^{-1} blue shift for an isolated ^{13}C-amide carbonyl.[44] IR simulations predict a ^{13}C-carbonyl blue shift when carbonyl oscillators are aligned and proximal,[36,38] an alignment uniquely satisfied by nanotube F19 carbonyls in the registry-shifted β-sheets identified by solid-state NMR (Figure 3b,c). In addition, the ^{13}C-labeled A21 amide I band in nanotubes is quite broad, from 1620 to 1614 cm^{-1}, consistent with multiple backbone environments that may arise from the less restrained methyl side-chain packing at the peptide termini.

The absolute ^{13}C frequency shift is inversely dependent on the distance between the adjacent ^{13}C carbonyls (r^{-3}) in nanotubes (Figure S4), indicating the importance of static dipole−dipole interactions. However, the fiber ^{13}C frequency shifts are independent of the ^{13}C carbonyl distances (Figure S4). The ^{13}C-labeled oscillators in adjacent fiber peptide strands have opposite orientations (Figure 3b, left), resulting in a smaller contribution to the overall coupling. Therefore, the transition dipole coupling between ^{13}CO oscillators is not merely distance-dependent, and interpretation of the spectra simply on the basis of the absolute ^{13}C component shift[38] could be misleading. Taken together, these NMR and IR assignments place significant constraints on the overall architecture and highlight differences between the fiber and nanotube β-sheet faces.

Figure 3b−d summarizes these backbone assignments for both Aβ(16−22) fibers and nanotubes, and the resulting macromolecular models are shown in Figure 5. A 50 Å diameter compact cross-β amyloid fiber requires five β-sheets stacked 9.9 Å apart along the x-orientation. Along y, with the length of an Aβ(16−22) peptide β-strand of 23 Å, each β-sheet would minimally consist of two end-to-end peptides (Figure 5a). Likewise, to account for the 43 Å thick wall of the nanotube (Figure 5c), each β-sheet must include a peptide bilayer.[17] However, unlike the typical fiber cross-β architecture, the peptide β-sheets are not oriented parallel to the fiber long axis. Rather, the β-sheets are arranged in a helical coiled fashion (Figure 5c), and, as diagrammed in Figure 5d, each wall of a collapsed nanotube would give a cross-β pattern offset by the helical pitch angle, ∼23° from the nanotube long axis, as seen by electron diffraction (Figure 2b). The Aβ(16−22) nanotubes would then include ∼150 β-sheets along x (Figure S5), accounting for the significantly stronger 9.9 Å reflection also observed in the electron diffraction of oriented nanotubes. Two of the four largest exposed fiber surfaces consist of exposed side chains (Figure 5a), whereas, except at the ends of the tube, all the side chains are buried in the nanotubes (Figure 5c).

3D Structure. While the repeating unit for both fibers and nanotubes can be represented by the four peptide strands in Figure 5b, the determined backbone registry indicates that the β-sheet faces are dramatically altered. Specifically, fiber β-sheets have both a polar and a nonpolar face, while tubes have the same side chains displayed on each face (Figure 3d), as the registry-shifted peptide must also be rotated to preserve intermolecular H-bonds. To determine the specific contacts and electrostatic interactions (H-bonds, salt bridges, etc.) between

(36) Paul, C.; Wang, J.; Wimley, W. C.; Hochstrasser, R. M.; Axelsen, P. H. *J. Am. Chem. Soc.* **2004**, *126*, 5843–5850.
(37) Hiramatsu, H.; Goto, Y.; Naiki, H.; Kitagawa, T. *J. Am. Chem. Soc.* **2005**, *127*, 7988–7989.
(38) Paul, C.; Axelsen, P. H. *J. Am. Chem. Soc.* **2005**, *127*, 5754–5755.
(39) Silva, R. A. G. D.; Barber-Armstrong, W.; Decatur, S. M. *J. Am. Chem. Soc.* **2003**, *125*, 13674–13675.
(40) Brauner, J. W.; Dugan, C.; Mendelsohn, R. *J. Am. Chem. Soc.* **2000**, *122*, 677–683.
(41) Kubelka, J.; Keiderling, T. A. *J. Am. Chem. Soc.* **2001**, *123*, 6142–6150.
(42) Bour, P.; Keiderling, T. A. *J. Phys. Chem. B* **2005**, *109*, 5348–5357.
(43) Miyazawa, T. *J. Chem. Phys.* **1960**, *32*, 1647–1652.
(44) Halverson, K.; Sucholeiki, I.; Ashburn, T. T.; Lansbury, R. T. *J. Am. Chem. Soc.* **1991**, *113*, 6701–6703.

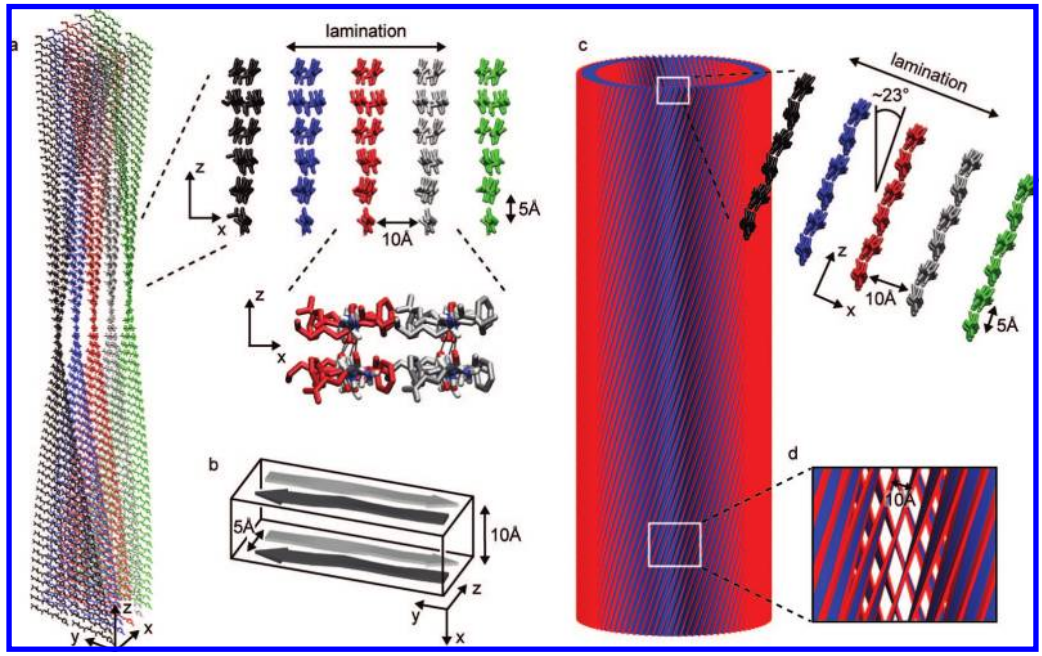

Figure 5. (a) Aβ(16−22) amyloid fiber cross-β architecture. Five β-sheets are arranged with the peptides perpendicular to the fiber z-axis. Interchain H-bonds, forming β-sheets, run parallel to the fiber z-axis. Peptides of each β-sheet are individually colored and have a pitch of 1.6°. In the expansions, typical amyloid sheet-stacking or lamination (10 Å) and H-bonding (5 Å) distances are indicated. Interacting side chains for four peptides in adjacent laminates are shown in the bottom expansion. (b) Minimal unit cell, with β-strands depicted as arrows, consisting of two β-sheets each with two H-bonded β-strands to describe macromolecular assemblies. The final morphology can be controlled by manipulating growth along x, y, and z. The β-sheet growth/H-bond dimension with peptide spacing of 5 Å is along the z-axis. β-Sheet stacking/lamination with peptide spacing of 10 Å is along the x-axis, and β-strand extension is along the y-axis. (c) Aβ(16−22) pH 2 nanotube. A total of 130 β-sheets laminate and coil up into ribbons to form nanotubes, resulting in individual H-bonded β-sheets running at an angle of ~23° with respect to the tube axis. (d) Expansion showing β-sheet tilt of the front and back nanotube walls. In the blue/red tube schematic, the exposed edges of the β-sheets are colored red and the interior is blue.

β-sheets, MD simulations on solvated models of five β-sheets with five peptides each were constructed for various sheet orientations (Figure S6). Except to define the H-bonded β-sheet peptide registry, no experimental NMR or X-ray restraints were used during the MD simulations. Rather, short (~1 ns), unrestrained MD with the OPLS-AA (all atom) force-field[30] at 300 K in an octahedral box of ~9000 SPC[29] water molecules was used to explore the energy landscape for local minima. Only peptides from the central 3 × 3 core were analyzed to minimize artifacts arising from edge effects, and no water molecules were found in either model of the fiber or nanotube β-sheet–β-sheet interfaces as a result of the tight packing of peptide side chains.

Only a single fiber model was identified from the MD conformational trajectory that was consistent with the XRD β-sheet lamination distance of 9.9 Å (Figures 6 and S7). The peptides in adjacent sheets are parallel, resulting in the polar and nonpolar β-sheet faces interacting with each other (Figures 6 and S6). As shown in Figure 6b, the MD model reveals that charge stabilization between residues K and E occurs along each individual fiber β-sheet face. This model suggests that the 50 Å diameter fiber in Figure 5a has a polar and nonpolar face, which may lead to the formation of the twisted fiber dimers shown in TEM micrographs (Figure 1a). In contrast, the symmetric β-sheet faces created by the single registry shift in the peptide nanotubes (Figure 3d) allows multiple sheet−sheet stacking orientations (e.g., parallel or antiparallel, not shown) in the MD simulations to achieve the 9.9 Å sheet stacking distance. As a result of the registry shift, no K−E electrostatic interactions occur within a sheet. These interactions are also absent between adjacent β-sheets in the MD models. This positional difference is reflected in the standard deviation of atom coordinates when the nine fiber and nanotube peptide

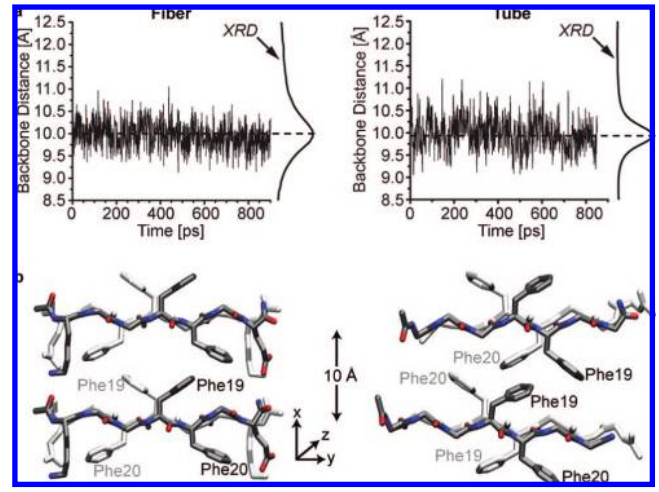

Figure 6. Molecular dynamics results for Aβ(16−22) (Ac-KLVFFAE-NH_2) in-register antiparallel β-sheet fibers (left) and out-of-register antiparallel β-sheet nanotubes (right). (a) Representative MD sheet−sheet distances. On the right-hand side of each graph is the corresponding WAXS powder diffraction data. (b) Four peptides representing two sheets of two H-bonded peptides as in Figure 5b, showing only backbone and F19/F20 side-chain atoms for the nanotube (right) and also the polar K17 and E22 side chains for the fiber (left). The H-bonded peptides farthest from view are colored white.

strands from the 3 × 3 core of each MD simulation are superimposed (Table 1). In the fiber β-sheets, the smaller root-mean-square deviation for K16 is consistent with a more ordered side chain resulting from the cooperative K−E electrostatic interaction.

The intersheet buried surface areas between H-bonded peptide dimers are similar, 369 ± 31 and 377 ± 44 Å^2, averaged over

Table 1. Root-Mean-Square Deviation (in Å) for Aβ(16−22) of C, N, and O Atoms for the Nine Peptide Strands of Fiber and Nanotube MD Models

	all	K	L	V	F	A	E
fiber	1.0	0.9	1.1	0.7	0.9	0.5	1.3
tube	1.1	1.5	0.8	0.7	0.8	0.4	1.2

the four 2 × 2 peptide units in the 3 × 3 core for the fibers and nanotubes, respectively. However, the lipophilic potential[45,46] changes upon protonation of the E22 side chain at acidic pH. In Figure 7, the lipophilic potential is mapped onto the calculated solvent-accessible surface area for a H-bonded peptide dimer of the central 3 × 3 core. Not only do the nanotube peptide dimer MD models have a larger hydrophobic surface area than the fibers, but the lipophilic potential for the top and bottom β-sheet faces are complementary for the tubes and not for the fibers.

The fiber and nanotube models from Figure 6 were used to create five infinitely long β-sheets by setting the MD simulation box length equal to the distance for six H-bonded peptides. Periodic boundary conditions then force the β-sheets to be flat. The resulting nanotube MD sheet−sheet distances matched the XRD distance of 9.9 Å, whereas the fiber MD simulations did not (data not shown), supporting the flat β-sheets in the nanotubes and twisted β-sheets in the fibers depicted in Figure 5.

Discussion

While prions can manifest as stable biological strains that self-propagate in non-Mendelian distributions, the structural basis for these epigenetic effects remains undefined. In this context, the central core peptide of Aβ, residues 16−22, is remarkable in both its ability to form different morphologies and the subtle change in conditions necessary to switch between fibers and nanotubes. At neutral pH, both K16 and E22 residues are charged, and the K−E salt-bridge appears to direct antiparallel and in-register β-sheet assembly. At pH 2, the formal charge on E22 is removed, and one H-bonded residue is sacrificed in the assembly of out-of-register antiparallel peptide β-sheets. Cross-seeding experiments, adding fiber seeds to nanotubes or *vice versa*, did not alter the final observed morphology. This observation argues that solution conditions set the nucleating center and dictate final morphology.

The simplicity of the assertion that a single salt bridge mediates the preference for fiber assembly was tested with Aβ(16−22)E22L (Ac-KLVFFAL-NH_2), a peptide containing a neutral replacement for the C-terminal glutamate. TEM analysis of the Aβ(16−22)E22L peptide assemblies found homogeneous diameter nanotubes at both pH 2 and pH 6 (Figure S8), and ssNMR distance measurements, using a labeling scheme identical to that in Aβ(16−22), [1-^{13}C]L17 [^{15}N]A21 (Figure S9), established that Aβ(16−22)E22L nanotubes at both pH values form identical antiparallel, out-of-register β-sheets. Moreover, SAXS analyses showed that, just like Aβ(16−22), these assembled E22L nanotubes retained the 4 nm thick wall, a sheet lamination distance of 10.4 Å, and a monodisperse tube diameter of 380 Å (Figure S10).

Without a dominant salt bridge, the structural data reveal several other factors which contribute to nanotube assembly.

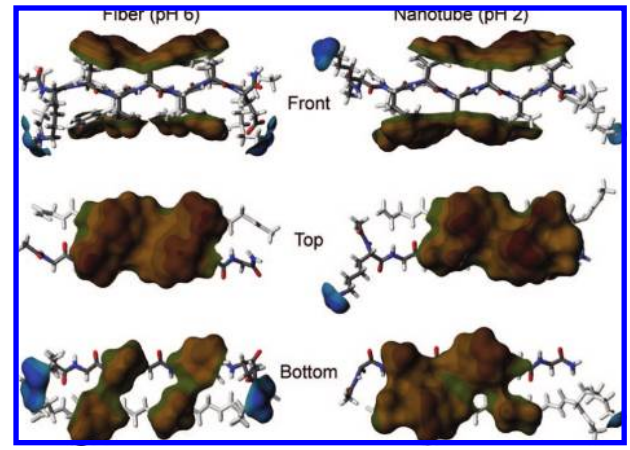

Figure 7. Lipophilic potential surface for in-register antiparallel β-sheet fibers (left) and out-of-register antiparallel β-sheet nanotubes (right) of peptide dimers. Brown indicates lipophilic, blue indicates hydrophilic, and green indicates neutral. In the top and bottom views, only the top or bottom side chains and solvent-accessible surface areas are shown.

First, the β-sheet faces of the minimal repeating unit of the fiber have different numbers of side chains, six vs eight (cf. Figure 3d), with a pseudo-C_2 symmetry axis, defined with respect to side-chain type and not atom position, perpendicular to the β-sheet plane. In the fibers, adjacent strands have polar residues K16 and E22 positioned on the same β-sheet face, creating polar and nonpolar surfaces with intrasheet salt bridges in the MD models. In contrast, the single residue-shifted registry of the nanotubes reduces the number of H-bonded residues to six, and the H-bonded two-strand minimal repeating unit of the nanotubes approximates an inversion center of symmetry. This arrangement places an equal number of side chains on each face (seven each) and positions K16 and E22 of adjacent strands on opposite β-sheet faces. Cross-sheet pairing of residues E and K could stabilize laminate association, and indeed such interactions have been found with metal ion coordination,[47] where the metal stabilizes sheet lamination and leads to the growth of nanotubes. However, neither the E22L congener peptide nor the MD data support an intersheet K−E interaction as being a driving force for nanotube β-sheet lamination. Rather, the symmetric nature of the faces as observed in the nanotube MD models appears to contribute significantly to lamination.

Second, MD simulations predict aromatic stacking within the Phe-Phe core (Figures 3d and 6b, right) that includes edge-to-face interactions[48] between F19/F20 in the fibers and F19/F19 and F20/F20 in the tubes. However, in the nanotubes, a third Phe-Phe offset stacked interaction appears between adjacent strands from different sheets (e.g., between white and gray F19's in Figure 6b, right). This packing interaction is uniquely found in the tube models and appears to contribute to both the lamination and β-sheet association in the form of a Phe zipper. A similar Phe zipper has been observed in fibrous nanocrystals of KFFEAAAKKFFE in stabilizing β-sheet lamination.[49] To test the importance of this FF dyad in Aβ(16−22) nanotube assembly, these residues were replaced with YY, WW, and II dyads. Under identical assembly conditions, only peptides containing the II residues assembled, but into fibers and not

(45) Ghose, A. K.; Viswanadhan, V. N.; Wendoloski, J. J. *J. Phys. Chem. A* **1998**, *102*, 3762–3772.
(46) Heiden, W.; Moeckel, G.; Brickmann, J. *J. Comput.-Aided Mol. Des.* **1993**, *7*, 503–514.
(47) Dong, J.; Shokes, J. E.; Scott, R. A.; Lynn, D. G. *J. Am. Chem. Soc.* **2006**, *128*, 3540–3542.
(48) Waters, M. L. *Curr. Opin. Chem. Biol.* **2002**, *6*, 736–741.
(49) Makin, O. S.; Atkins, E.; Sikorski, P.; Johansson, J.; Serpell, L. C. *Proc. Natl. Acad. Sci. U.S.A.* **2005**, *102*, 315–320.

nanotubes. Therefore, the complementarity of this Phe zipper interaction appears to contribute to lamination and play a greater role in stabilizing the nanotubes.

Finally, similar side-chain complementarity has been observed in microcrystals of amyloid-forming peptide segments[9] as well as in interacting α-helix surfaces,[50–52] where these associations mediate inter-helix crossing angles.[53] β-Sheet stacking distances depend on the size of the side chain, from 3.7 Å for polyglycine[54] to 14 Å for calcium salts of polyglutamic acid.[55] In amyloid fibers, a sheet-stacking distance in the middle of this range, 10 ± 1 Å, is generally observed,[56] further highlighting the importance of side-chain complementarity within the tightly packed repeating units of these assemblies.

Taken together, the amino acid side-chain arrangements, most easily seen in the lipophilic surfaces of the MD models and their complementary packing within the β-sheet faces, appear to drive the peptide registry and β-sheet planarity essential to the minimal repeating unit cell of nanotube assembly. We previously predicted that each amino acid maintained in planar H-bonded β-sheet arrays contributes ≥2 kcal/mol in strain energy.[57] Twisting of the fiber β-sheet compensates for this strain energy within the seven-residue H-bonded backbone, quite possibly dictating the twisting topology of the fibers. In contrast, six-residue H-bonded β-sheets have lower strain energy, hence creating the flat sheets that allow for the increased number of laminates required for the helical coiled topology leading to nanotubes. Indeed, when this facial complementarity is supplemented with metal binding sites, metal coordination drives nanotube morphology of even longer peptides.[15,47,58]

Most remarkable is the realization that a simple shift in peptide registry of Aβ(16−22) β-sheets can so profoundly alter the surface complementarity of the nucleating center. Given the segmental nature of many, if not all amyloidogenic proteins,[8] such subtle changes in even one nucleating event could propagate throughout the protein and allow for a rich diversity of amyloid/prion strains, each competing for survival within the cellular compartment. Indeed, subtle changes in the simple cassettes themselves are sufficient to emulate the early events in Aβ-induced neuronal degeneration.[15] One can now imagine that this cassette architecture offers a rich tapestry for regulating the tertiary and quaternary structure of protein self-assemblies and for the creation of self-assembled morphologies of unprecedented complexity.

In a manner similar to covalent modifications seen in epigenetic regulation of gene expression, the addition of a single proton to Aβ(16−22) changes the accessible conformational states to enable the growth of nanotubes. For amyloid assemblies, simple changes in environmental conditions[15,47,58] could give rise to rich assortments of distinct assemblies that may well underlie the observed biological structure. The nucleation of Aβ(16−22) then reveals a first step in our growing ability to select from within this wide tapestry of possible structures for the creation of topologically complex supramolecular self-assemblies.

Acknowledgment. We are indebted to Dr. Robert Apkarian for assistance with cryo-EM, Jeannette Taylor for assistance with electron diffraction, and Matt Geballe for advice on MD. Microscopy images were collected at IM&MF, Emory University. We acknowledge the assistance of Dr. Soenke Seifert, XSD, APS in the SAXS and WAXS measurements. This work benefited from use of the APS and IPNS funded by the U.S. DOE, BES under contract DE-AC02-06CH11357 to the University of Chicago, DOE (ER15377) and NSF (CRC-CHE-0404677) for support, and NSF(CHE-0131013) for CD instrumentation.

Supporting Information Available: XRD, CD, $^{13}C\{^{15}N\}$ REDOR dephasing, and isotope-edited IR peak positions; $^{12}C-^{13}C$ splitting as a function of ^{13}CO distance of Aβ(16−22) fibers and nanotubes; calculation of number of β-sheets in Aβ(16−22) nanotubes; schematic of initial sheet−sheet orientations and sheet−sheet distances in Aβ(16−22) fiber MD simulations; TEM and $^{13}C\{^{15}N\}$REDOR dephasing of Aβ-(16−22)E22L nanotubes. This material is available free of charge via the Internet at http://pubs.acs.org.

JA801511N

(50) Crick, F. H. C. *Acta Crystallogr.* **1953**, *6*, 689–697.
(51) Chothia, C. *Annu. Rev. Biochem.* **1984**, *53*, 537–572.
(52) Langosch, D.; Heringa, J. *Proteins* **1998**, *31*, 150–159.
(53) Walters, R. F. S.; DeGrado, W. F. *Proc. Natl. Acad. Sci. U.S.A.* **2006**, *103*, 13658–13663.
(54) Fraser, R. D. B.; Gillespie, J. M.; Macrae, T. P. *Comp. Biochem. Physiol. B* **1973**, *44*, 943–947.
(55) Keith, H. D.; Padden, F. J., Jr.; Giannoni, G. *J. Mol. Biol.* **1969**, *43*, 423–438.
(56) Sikorski, P.; Atkins, E. D.; Serpell, L. C. *Structure* **2003**, *11*, 915–926.
(57) Morgan, D. M.; Lynn, D. G.; Lakdawala, A. S.; Snyder, J. P.; Liotta, D. C. *J. Chin. Chem. Soc.* **2002**, *49*, 459–466.
(58) Morgan, D. M.; Dong, J.; Jacob, J.; Lu, K.; Apkarian, R. P.; Thiyagarajan, P.; Lynn, D. G. *J. Am. Chem. Soc.* **2002**, *124*, 12644–12645.
(59) Gehman, J. D.; Separovic, F.; Lu, K.; Mehta, A. K. *J. Phys. Chem. B* **2007**, *111*, 7802–7811.